Valorization of hazelnut shell waste biomass into sustainable carbons for energy storage applications

Waste Management 213 (2026) 115363

Contents lists available at ScienceDirect

Waste Management

journal homepage: www.elsevier.com/locate/wasman

Research Paper

Valorization of hazelnut shell waste biomass into sustainable carbons for energy storage applications

Stefania Volante [a], Rif Atussaufiyah [b], Federico Maria Vivaldi [a], Pietro Zaccagnini [b,c], Mara Serrapede [b,c], Andrea Lamberti [b,c], Anna Maria Raspolli Galletti [a,d], Federico Bella [b,c], Fabio Di Francesco [a], Domenico Licursi [a,d], Claudia Antonetti [a,d,*]

[a] Department of Chemistry and Industrial Chemistry, University of Pisa, Via G. Moruzzi 13, 56124 Pisa, Italy
[b] Department of Applied Science and Technology, Politecnico di Torino, Corso Duca Degli Abruzzi 24, 10129 Turin, Italy
[c] Center for Sustainable Future Technologies, Istituto Italiano di Tecnologia, Via Livorno 60, 10144 Turin, Italy
[d] Consorzio Interuniversitario Reattività Chimica e Catalisi (CIRCC), Via Celso Ulpiani, 27, 70126 Bari, Italy

ARTICLE INFO

Keywords:
Hazelnut shells valorization
Hydrochars, pyrochars, activated carbons
Copper oxide doping
Lithium-ion storage
Supercapacitors

ABSTRACT

In the last decades, the use of biochar has been receiving increasing attention for the development of electrochemical energy storage devices. In this work, the waste hazelnut shell biomass, a low cost and abundant agriculture residue within our territory, was valorized as feedstock for the synthesis of alkali-derived activated carbons, which were properly characterized and electrochemically tested, in the perspective of their use as new electrode material in energy storage applications. Two activated carbons have been identified as promising materials for this application and their electrochemical performances were further improved by including a doping step with copper (I) oxide, achieving the best specific capacitance of 123 F/g. Moreover, one of the two most promising activated carbons was tested in an EDLC symmetric device outperforming, at low power rates, reference materials in terms of specific energy density, reaching the value up to 40 Wh/kg, due to its remarkable specific capacitance of 55 F/g. In summary, this work proposes a sustainable and low energy demanding approach to transform waste biomasses into high value activated carbon materials for energy storage applications. The strategy not only promotes the reuse and valorization of hazelnut shell waste biomass, but it also supports a circular model with promising environmental and economic advantages.

1. Introduction

The global demand for energy is steadily increasing, driving intense research into alternative and renewable energy sources, particularly those derived from waste materials, such as biomasses (Bhat et al., 2023). Within the clean energy landscape, electrochemical energy plays a pivotal role in replacing fossil fuels. In this context, devices such as supercapacitors (SCs), batteries and fuel cells have emerged as efficient solutions, each relying on distinct electrochemical conversion mechanisms. Among these, SCs are gaining growing attention due to their high specific capacitance (C_s), long cycle life, high power density, low maintenance, absence of memory effect and improved safety (Lobato-Peralta et al., 2024; Poonam et al., 2019). SCs are generally classified on their charge storage mechanism into electric double-layer capacitors (EDLCs) and pseudocapacitors (Yuan et al., 2024). In EDLCs the energy is stored via the electrostatic accumulation of ions at the electrode/

Abbreviations: SCs, Supercapacitors; C_s, Specific capacitance; EDLCs, Electric double-layer capacitors; HCs, Hybrid capacitors; SSA, Specific surface area; ACs, Activated carbons; CNTs, Carbon nanotubes; HTC, Hydrothermal carbonization; MOFs, Metal-organic frameworks; COFs, Covalent organic frameworks; HS, Hazelnut shell; PVDF, Polyvinylidene fluoride; CB, Carbon black; SBR, Styrene butadiene rubber; CMC, Sodium carboxymethyl cellulose; $LiPF_6$, Lithium hexafluorophosphate; EC, Ethylene carbonate; DMC, Dimethyl carbonate; VC, Vinylene carbonate; LP30, 1 M $LiPF_6$ in EC : DMC 1:1 (v:v) + 2 wt% VC; $TEABF_4$, Tetraethylammonium tetrafluoroborate; PC, Propylene carbonate; CuOAc, Copper (II) acetate; SEM-EDS, Scanning electron microscopy-Energy dispersive spectroscopy; BET, Brunauer-Emmett-Teller; NLDFT, Non-local density functional theory; ICP-OES, Inductively coupled plasma optical emission spectroscopy; XRD, X-ray diffraction; NMP, N-methyl-2-pyrrolidone; CV, Cyclic voltammetry; GCD, Galvanostatic charge-discharge; EIS, Electrochemical impedance spectroscopy; V_{micro}, Micropore volume; A_{micro}, Micropore area; V_{meso}, Mesopore volume; A_{ext}, External area; ACN, Acetonitrile.

* Corresponding author at: Department of Chemistry and Industrial Chemistry, University of Pisa, Via G. Moruzzi 13, 56124 Pisa, Italy.
E-mail address: claudia.antonetti@unipi.it (C. Antonetti).

https://doi.org/10.1016/j.wasman.2026.115363
Received 4 September 2025; Received in revised form 14 December 2025; Accepted 19 January 2026
Available online 29 January 2026

electrolyte interface, whereas pseudocapacitors operate through rapid, reversible redox reactions, involving faradaic charge transfer between electrode and electrolyte (Poonam et al., 2019). When SCs and batteries' electrodes are combined in the same device or when SCs and batteries' materials are combined in the electrode, the resulting device is called hybrid capacitors (HCs), which simultaneously offer high energy and high power densities (Wang et al., 2021; Mascarenhas et al., 2023).

Carbon-based materials are widely used in EDLC electrodes due to their high specific surface area (SSA), chemical stability and electrical conductivity. Among them, carbon aerogels (Pedico et al., 2018), activated carbons (ACs) (Lan et al., 2020), carbon nanotubes (CNTs) (Dangbegnon et al., 2023) and graphene (Reina et al., 2023) are the most common ones and in particular ACs obtained from biomasses are a promising solution in a circular economy perspective. In fact, biomass is attracting high interest and has proven to be a promising alternative as a renewable source of many carbon-based materials, being characterized by a carbon backbone that allows for its effective use in various scientific and technological applications (Hegde and Bhat, 2023). Adopting different thermal treatments, biomass can be converted into bio-carbons (or "biochars"), whose properties depend on the feedstock composition and processing conditions (Inagaki et al., 2010; Poonam et al., 2019). Two widely studied thermal processes for biomass conversion are pyrolysis and hydrothermal carbonization (HTC), but these often result in limited SSA (Borchardt et al., 2014; Poonam et al., 2019; Yuan et al., 2024). To enhance porosity and performances, physico-chemical activation is typically required (Yuan et al., 2024; Hegde et al., 2024). Physical methods involve gases such as steam or CO_2, while chemical activation uses agents such as H_3PO_4, KOH, and $ZnCl_2$ (Poonam et al., 2019; Gao et al., 2020). Among these, KOH has emerged as the preferred activating agent, producing ACs with high SSA and well-tuned micro/mesoporous structures, fundamental aspect for EDLC functional role (Poonam et al. 2019; Yuan et al. 2024). In this context, a wide range of biomass wastes have been investigated for the preparation of ACs intended for energy storage application, due to their easy availability, less complex preparation processes compared to other materials and good electrochemical performances, mainly evaluated in terms of C_s, which generally resulted in the range 200–400 F/g, as reported in Table S1 (Hegde and Bhat, 2023; Elmouwahidi et al., 2017; Subramani et al., 2017; Yang et al., 2019; Zhan et al., 2021a). In this regard, interesting studies were performed by adopting KOH as the activating agent starting from wood sawdust, peanut shell, orange peels and Tasmanian blue gum, reaching in all cases good C_s (Tests 1–4, Table S1). A notable example is reported by Yang *et al.* (Yang et al., 2019), who used wood sawdust as starting feedstock to produce ACs via HTC (pre)-treatment in the presence of KOH, followed by thermal pyrolysis treatment (Test 1, Table S1). The obtained AC was electrochemically tested using a three-electrode workstation in KOH 6 M electrolyte, achieving the high C_s of about 300 F/g at 1 A/g. Another promising study, employing KOH as activating agent, is performed by Zhan *et al.* (Zhan et al., 2021b) who proposed peanut shells as starting feedstock, preliminary carbonized at 600 °C and then chemically activated at 800 °C (Test 2, Table S1), achieving the highest C_s value of about 340 F/g at 1 A/g in a three-electrode system with 6 M KOH. In addition to the most used KOH, other activating agents have been reported in the literature, such as H_3PO_4 and K_2CO_3, employed respectively starting from olive residues and coconut shell, achieving lower C_s than those obtained with KOH (Tests 5–6, Table S1).

Today one abundant waste biomass yet underutilized for energy storage applications is hazelnut shell (HS), a waste product constituting over 50 wt% of the hazelnut, with global production exceeding 585,000 tons in 2023 (Statista, 2025; Pérez-Armada et al., 2019). HS wastes are highly concentrated in the European union territory due to their intense production in Turkey and Italy, that is respectively 64 and 8% of global production in 2021 (Hazelnut Hub, 2025). HS has been up to now valued for heat or chemicals production (Licursi et al., 2023) and more recently for the synthesis of ACs for energy devices. In this regard, Xie *et al.* (Xie et al., 2021) reported the high C_s of 240 F/g from HS using a multi-step activation combining KOH and $Zn(NO_3)_2$, reaching SSA values of 1096 m^2/g. This performance aligns with top commercial EDLCs (~250 F/g) (Olabi et al., 2023), for which, however, the energy density remains a limit, reaching values about 2.3–8 Wh/kg (Pathak et al., 2024) in comparison to 200–300 Wh/Kg for lithium ion batteries, highlighting the need for further improvements (Poonam et al., 2019; Pathak et al., 2024). To overcome the limitations of ACs, researchers have explored pseudocapacitors, incorporating metal oxides, such as RuO_2 (Zheng et al., 1995) and IrO_2 (Beknalkar et al., 2021), both capable of reaching C_s values of about 700 F/g and considered in literature, up to now, as two of the best examples. Other metal oxides have been explored, including NiO, MnO_2 and Fe_2O_3 (Zhan et al., 2021b; Aziz and Shah, 2023), however the use of these oxides as the only component of the electrode may involve limitations since they exhibit low conductivities, which reduce their efficiency during fast charging/discharging, negatively affecting both the rate performances and C_s (Chen and Xue, 2013). In addition to transition metal oxides, other materials have also been considered for electrode fabrication, such as metal–organic frameworks (MOFs), covalent organic frameworks (COFs) and conductive polymers (Bhojane, 2022). These materials, similar to metal oxides, also show several disadvantages when used as bulk electrode materials, mainly due to their low intrinsic electrical conductivity and limited stability under repeated cycling (Sajjad and Lu, 2021; Ansari et al., 2024; Dallaev, 2025). For this reason, one possible solution is to obtain composite materials including metal oxides, MOFs, COFs or conductive polymers or use the last ones as doping agents for AC, thus achieving a more stable material (Sajjad and Lu, 2021; Ansari et al., 2024; Dallaev, 2025). Among emerging options, copper oxides, only preliminary discussed in literature, offer a promising balance of cost, conductivity, high theoretical pseudocapacitance and good availability (Aziz and Shah, 2023; Chen and Xue, 2013; Moosavifard et al., 2015). However, copper oxides suffer from agglomeration and degradation during cycling (Aziz and Shah, 2023), but combining them with ACs, it is possible to exploit synergistic effects of redox activity enhancement of copper oxides and mechanical degradation mitigation of ACs, thus improving device lifespan (Aziz and Shah, 2023). In this context, Saravanakumar *et al.* (Saravanakumar et al., 2019) claimed the highest C_s of 600 F/g employing the composite material made up of mesoporous carbon together with copper (II) oxide. However, such high C_s requires the employment of a high CuO loading (22 wt% as Cu), whereas the AC component plays only a minor role. Zhan *et al.* (Zhan et al., 2021b) also employed CuO as doping agent for a peanut shell-derived AC, where in this case, AC represented the main component of the electrode (5 wt% as Cu), claiming the highest capacitance of 500 F/g. Although the very good values obtained for C_s, the synthesis of this Cu-doped AC was performed adopting three cascade steps: 1) a carbonization one (pyrolysis at 600 °C for 3 h), 2) a KOH activation one (800 °C for 2 h) and 3) a calcination one (310 °C for 2 h), overall resulting in a highly-energy demanding procedure (Zhan et al., 2021b). Based on the above discussion, the present study explores in energy storage applications the use of the waste HS biomass-derived biochars, synthesized according to our previous work (Licursi et al., 2023) adopting a milder three-step thermal protocol: 1) HTC (220 °C, 5 h), 2) pyrolysis (600 °C, 1 h), and 3) activation pyrolysis (600 °C, 1 h), yielding several types of biochars, including, hydrochars, pyrochars and ACs depending on the performed steps. This approach is less energy-intensive than Zhan's (Zhan et al., 2021b), especially in terms of temperature. The 3-step procedure enabled us to obtain the AC called PYRO-AC, and then two other ACs were produced: HS-AC (direct activation of raw HS) and HTC-AC (activation of HTC-derived char), as shown in Fig. 1. In addition, a non-activated pyrochar (HTC-PYRO) was also considered for comparison. All the synthesized samples were electrochemically tested, and the best ones were further modified with copper oxides doping, exploiting a synergy rarely studied in literature for improved performances, paying attention to the structural properties of the obtained materials.

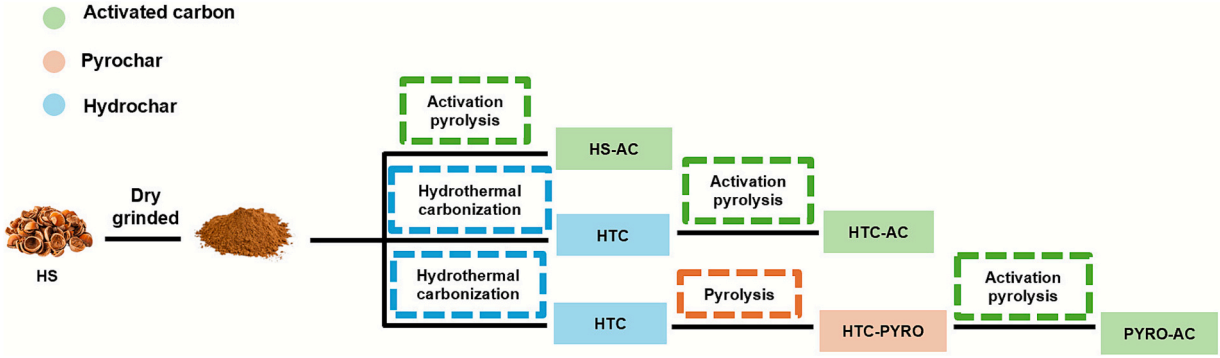

Fig. 1. Proposed strategies for the synthesis of ACs from hazelnut shells from a cascade approach with the intermediate production of hydrochars and pyrochars: HS-AC from raw biomass; HTC-AC from hydrochar (HTC); PYRO-AC from pyrochar (HTC-PYRO). In addition, the pyrochar HTC-PYRO from pyrolysis of hydrochar (HTC) was also considered. Reaction conditions: a) activation pyrolysis: precursor/KOH weight ratio of 1/4, heated at 600 °C for 1 h under 500 mL/min N_2 flow; b) hydrothermal carbonization: biomass loading of 20 wt% heated at 220 °C for 5 h; c) pyrolysis: heated 600 °C for 1 h under 500 mL/min N_2 flow.

Definitely, this study shows an environmentally sustainable and low energy demanding cascade approach of increasing complexity to valorize HS in energy storage applications, resulting an example of circular economy approach. In particular, the present research effectively demonstrates the conversion of an agro-industrial by-product into a high functional material with promising electrochemical performances, highlighting the importance of resource recovery and the promotion of sustainable practices.

2. Materials and methods

2.1. Materials

HS biomass of *Tonda Gentile Romana* variety was kindly provided by Stelliferi-Itavex S.p.A., Caprarola, Viterbo (VT), Italy. According to our previous work (Licursi et al., 2023), this biomass is composed of cellulose (22.9 wt%), hemicellulose (23.5 wt%), Klason lignin (37.6 wt%), uronic acids (5.0 wt%), ash (1.4 wt%), ethanol-extractives (1.4 wt%) and others (8.2 wt%). Potassium hydroxide, sodium hydroxide, copper (II) acetate, hydrochloric acid and polyvinylidene fluoride (PVDF, Mw ~ 530.000) were purchased from Sigma-Aldrich. Potassium nitrate was purchased from Carlo Erba. 1-Methyl-2-pyrrolidinone (NMP) and carbon black acetylene were purchased from Thermo Scientific Chemicals. Nickel foam (surface area of 420 m^2/g and 1.6 mm thickness) was purchased from Tecnasa S.L. Madrid, Spain. Styrene butadiene rubber (SBR) and sodium carboxymethyl cellulose (CMC) were purchased from MIT Corporation. Lithium hexafluorophosphate ($LiPF_6$) solution 1 M in ethylene carbonate (EC): dimethyl carbonate (DMC) 1:1 (v:v) + 2 wt% of vinylene carbonate (VC) solvent mixture (LP30) was provided by Solvionic, the tetraethylammonium tetrafluoroborate ($TEABF_4$) was purchased by IoliTech, the solution in propylene carbonate (PC) and the Whatman glass fiber of grade D were provided by Sigma-Aldrich. All materials were used as received, without any pretreatments.

2.2. Synthesis of pristine and doped ACs

2.2.1. Synthesis of pristine ACs

Pristine ACs (HS-AC, HTC-AC and PYRO-AC) were synthesized starting from different carbon precursors, according to the chemical activation pyrolysis procedure already described in our previous work (Licursi et al., 2023). In details, for the activation pyrolysis, KOH, used as activating agent (precursor/KOH ratio = 1/4 wt/wt), was mixed directly with the selected precursor, working under the constant N_2 flow of 500 mL/min, employing the heating rate of 10 °C/min up to the set-point temperature of 600 °C, held at that value for 5 min. In a standard preparation, 2 g of carbon precursor were mixed with 8 g of KOH. All these ACs were washed with 10% (v/v) HCl, then by deionized water up to neutrality and lastly dried at 105 °C up to constant weight. Specifically, HS-AC sample was prepared by performing the activation pyrolysis directly on the starting biomass. HTC-AC sample required an HTC step performed for 5 h at 220 °C with the initial biomass loading 20 wt% (Licursi et al., 2017) before the activation pyrolysis, adopting for the HTC 37.5 g of starting biomass in 150 ml of water. Then, PYRO-AC was synthesized adding a further pyrolysis step, before the final activation pyrolysis, of the previous HTC sample, adopting for the added pyrolysis treatment the same reaction condition of the activation pyrolysis, but in the absence of the activating agent, which means in a standard preparation 2 g of carbon precursor with 8 g of KOH. Lastly, the HTC-PYRO sample was prepared performing the HTC treatment followed by the pyrolysis one, without the final activation pyrolysis procedure, both HTC and pyrolysis steps performed under the standard reported conditions.

2.2.2. Synthesis of Cu-doped ACs

The synthesis of Cu-doped ACs was performed with a slight modification of the procedures adopted by Saravanakumar and Zhan (Saravanakumar et al., 2019; Zhan et al., 2021b), using copper (II) acetate (CuOAc) as the copper precursor. In particular, 45 mg of CuOAc were dissolved in 10 mL of deionized water, then this solution was added to a round bottom flask containing 0.3 g of the selected AC and the resulting suspension was kept under constant stirring for 30 min. Afterwards, 2.5 mL of a 2 wt% NaOH solution were added to reach pH = 10 and the resulting suspension was stirred for 6 h at room temperature. At the end of this impregnation time, the product was recovered by centrifugation (15 min at 4000 rpm) and washed with deionized water up to neutrality. The resulting solid was subsequently heated in a muffle furnace at 150 °C for 2 h, in order to obtain the final Cu-derived product. Two Cu-doped ACs were synthesized according to this procedure: Cu-HTC-AC and Cu-PYRO-AC.

2.3. Physical chemical characterizations

Scanning electron microscopy (SEM-EDS) characterization was carried out using a FEI Quanta 450 FEG scanning electron microscope, equipped with a QUANTAX/EDS analysis system and QUANTAX XFlash Detector 6|10. The instrument operated under high vacuum conditions ($< 6e^{-4}$ Pa).

N_2 sorption isotherms were measured on Quantachrome Autosorb 1C instrument at 77 K on electrodes (active material onto current collector) previously outgassed at 200 °C for at least 4 h, to remove water and other atmospheric contaminants. From N_2 isotherms, the Brunauer-Emmett-Teller (BET) specific surface area (SSA) was measured by the multi-point method, working within the relative pressure (P/P0) range of 0.05–0.15. Micropore areas were calculated from the cumulative

surface area curves, obtained by the non-local density functional theory (NLDFT) method (kernel for nitrogen adsorption at 77 K onto carbon slit-pores). Microporous volume and external surface area were calculated by the t-plot statistical thickness method, using a CB thickness equation (fitted thickness range 0.35–0.44 nm).

Elemental analysis for the quantification of C, H, N and O content was performed using a Vario MICRO cube instrument (Elementar) equipped with a thermal conductivity detector. Oxygen content was calculated by difference, O (%) = 100 (%) – C (%) – H (%) – N (%) – ash (%).

Proximate analysis was carried out using a Q500 TA Instruments thermogravimetric analyzer. About 12 mg of each sample were weighed and heated to determine moisture and volatile matter, increasing the temperature from 30 to 900 °C, at the heating rate of 20 °C/min, under 100% of nitrogen flow. For the determination of fixed carbon and ash contents, the sample was then cooled from 900 to 800 °C under a nitrogen (40% v/v) and air (60% v/v) flow.

Inductively coupled plasma optical emission spectroscopy (ICP-OES) was performed using an ICAP 7000 series instrument (Thermo Fisher Scientific, USA) to determine the effective Cu content. The Cu-HTC-AC and Cu-PYRO-AC samples were previously microwave digested with HNO_3 and H_2O_2. In detail, the samples were heated to 80 °C, then to 110 °C, 130 °C and 160 °C, maintaining each temperature for 3 min. Finally, they were heated to 180 °C with a holding time of 20 min.

Micro-Raman spectroscopy was performed by using a Renishaw InVia Qontor Raman microscope. A laser diode source ($\lambda = 514$ nm) was used with 5 mW power, and sample inspection occurred through a microscope objective (20 ×), with a backscattering light collection setup. The Raman spectra were acquired in the range 140–2800 cm^{-1}. Data analysis and baseline corrections were performed by means of Fityk software (Wojdyr, 2010).

X-ray diffraction (XRD) measurements were carried out using a PANalytical Empyrean MRD Pro powder diffractometer equipped with a 1D PIXcel detector (Malvern PANalytical, United Kingdom). Diffractograms were collected in Bragg-Brentano reflection mode using Cu Kα radiation, at an operating voltage of 40 kV and a tube current of 30 mA. The instrumental broadening was calculated using the Caglioti equation based on the reflections of a standard LaB6 powder (NIST660a). Measurements were carried out in continuous mode with a step size of $2\theta = 0.0262°$ and a data time per step of 2000 s for all samples. MAUD software was used for quantitative analysis and refinement. The cif card matching the diffraction pattern of the copper oxide and the aluminum oxide in the composite are from COD database (Cu_2O: 1,010,963 and Al_2O_3: 9009680). The two broad peaks linked to the carbonaceous matrix of the samples were considered part of the background in the Rietveld refinement.

2.4. Electrochemical characterizations

The electrochemical evaluation involved various preparation methods and instrumentation setups. Reference and counter electrodes included Ag/AgCl and Pt wire, respectively. Electrolytes consisted of aqueous solutions of KOH and KNO_3 (each 2.5 M), as well as organic ones LP30 and 1 M $TEABF_4$ in PC.

Concerning the electrochemical tests in aqueous electrolytes, nickel foam (1 × 1 cm^2) current collector was treated in 0.1 M HCl using an ultrasonic bath for 1 h to remove surface oxides, then rinsed sequentially with acetone, ethanol and deionized water for three times. A slurry was prepared by mixing biochar (80 wt%), CB (10 wt%) and PVDF (10 wt%) in NMP (1 mL). This slurry was deposited on nickel foam and oven dried at 80 °C for 24 h. Concerning the electrochemical tests in organic electrolytes, copper and aluminum foil current collectors were coated using the doctor blade technique. The slurry was made by dissolving CMC in deionized water at 60 °C (0.1 mL water per 1 mg CMC), followed by gradual addition of CB and the selected active material under continuous stirring. After 2 h of mixing, SBR was added and stirred for an additional 2 h. The final slurry composition was active material (85 wt %), CB (10 wt%) and a 5 wt% binder blend (CMC:SBR = 1:2 wt/wt). Coated electrodes were air-dried, punched into 12 mm diameter discs for Swagelok T-cell testing and 16 mm for standard coin-cell 2032 format device tests. The electrode puncher was the pneumatic die cutter MSK-180S provided by MTI corp. The electrodes were vacuum dried at 120 °C for 8 h and transferred to a glove box for final processing under an argon atmosphere and cell assembly.

Electrochemical measurements were performed using an Autolab PGSTAT302N and BioLogic VMP3 instrument. Tests included cyclic voltammetry (CV), galvanostatic charge–discharge (GCD) and electrochemical impedance spectroscopy (EIS). CV was performed across varying potential windows and scan rates depending on the electrode system detailed in the following section. GCD tests were carried out on the individual positive and negative electrodes within their respective potential windows (1 to 0 V and −1 to 0 V) at the constant current of 0.03 A for 10 cycles. For EDLC applications, GCD measurements were carried out at 0.1–2.0 A/g to evaluate rate capability and at 1.0 A/g to assess cycling stability. The calculation of C_s by CV and GCD measurements is reported in the Supplementary Material. EIS was performed using a 5 mV sinusoidal signal over a frequency range from 1 MHz to 10 mHz.

3. Results and discussion

3.1. HS-derived biochars: physicochemical characterization and electrochemical behavior with aqueous electrolytes

The HS-derived biochars were initially synthetized and characterized. The samples HTC, HTC-PYRO and HS-AC were prepared according to our previous work (Licursi et al., 2023), whereas HTC-AC and PYRO-AC were synthesized and characterized for the target application (see Material and Methods). At the beginning, the morphological properties were evaluated for all the samples through SEM analysis. The SEM images of the precursors (HTC and HTC-PYRO) of the ACs together with the two ACs (HS-AC and PYRO-AC) were presented in our previous work (Licursi et al., 2023), whereas the SEM image of the HTC-AC sample is reported in Fig. S2 for completeness. The structure of the synthesized ACs (HS-AC, HTC-AC and PYRO-AC) is different to that of their corresponding precursors, exhibiting a finer structure and a more developed porosity, with a greater tendency toward micropore formation. The superficial properties also were evaluated, as shown in Table 1, underlining different values of SSA, micro- and mesopore volume, thus highlighting the impact of different treatments. The N_2 isotherm of new ACs (HTC-AC and PYRO-AC), together with the corresponding cumulative pore volumes and the pore size distribution are reported in Fig. S3. HTC exhibits the lowest SSA (11 m^2/g) and limited mesoporosity, as indicated by its low mesopore volume (0.066 cm^3/g). In contrast, the subsequent pyrolysis treatment (HTC-PYRO) increases the SSA to 388 m^2/g and promotes the development of a porous structure, as evidenced by a higher mesopore volume and the presence of microporosity. The subsequent chemical activation with KOH of the starting feedstock and the obtained biochars, resulted in the formation of the corresponding ACs (HS-AC, HTC-AC and PYRO-AC) which exhibited higher SSAs equal to 815, 1155 and 710 m^2/g, respectively, compared to their corresponding precursors. Moreover, an increase in micropore volume and area is observed for the ACs samples compared to their corresponding precursors (V_{micro} = 0.285 cm^3/g; A_{micro} = 721 m^2/g for HS-AC versus HS; V_{micro} = 0.454 cm^3/g; A_{micro} = 790 m^2/g for HTC-AC versus HTC and V_{micro} = 0.293 cm^3/g; A_{micro} = 511 m^2/g for PYRO-AC versus HTC-PYRO). Together with the increase in micropore volume and area in AC samples, a decrease in mesopore volume is observed (from 0.066 to 0.061 cm^3/g from HTC to HTC-AC and from 0.075 to 0.041 cm^3/g from HTC-PYRO to PYRO-AC). These findings indicate that sequential heat treatment induces the development of a microporous structure, a key characteristic for this application.

Table 1
Superficial properties (external area, mesopores volume, micropores area, micropores volume, SSA), ultimate analysis and proximate analysis of HS, HTC, HTC-PYRO, HS-AC, HTC-AC and PYRO-AC. Note: n.d. = not determined (absent in the sample); * samples characterized in our previous work (Licursi et al., 2023).

Characterizations		Starting feedstock	Biochar		Activated carbons		
		HS*	HTC*	HTC-PYRO*	HS-AC*	HTC-AC	PYRO-AC
Superficial properties	$Area_{ext}$ [m^2/g]	–	n.d	41	93	364	198
	$Volume_{meso}$ [cm^3/g]	–	0.066	0.075	0.110	0.061	0.041
	$Area_{micro}$ [m^2/g]	–	n.d.	347	721	790	511
	$Volume_{micro}$ [cm^3/g]	–	n.d.	0.138	0.285	0.454	0.293
	SSA [m^2/g]	–	11	388	815	1155	710
Ultimate analysis	C wt%	51.0	66.9	80.9	75.6	60.8	74.3
	H wt%	5.8	4.5	3.5	0.9	2.0	0.9
	N wt%	0.2	0.2	0.7	0.3	0.1	0.7
	O wt%	41.4	27.6	14.3	14.1	31.4	18.0
Proximate analysis	Ash wt%	1.6	0.8	0.6	9.1	5.7	6.1
	Fixed carbon wt%	22.4	45.5	81.2	68.1	60.8	69.4
	Volatile carbon wt%	76.0	53.7	18.2	22.8	33.5	24.5

Regarding the ultimate analysis data (Table 1), among the ACs, HTC-AC sample shows a limited carbonization progress (C = 60.8 wt%, H = 2.0 wt%, N = 0.1 wt%, O = 31.4 wt%) compared with that achieved with the other ACs (HS-AC and PYRO-AC), which carbon contents is in the range 70–80 wt% (Licursi et al., 2023). The still high oxygen content of HTC-AC indicates a moderate removal of oxygenated compounds during the HTC treatment and/or an oxygen enrichment resulting from the KOH activation treatment. This statement is further confirmed by the corresponding proximate analysis data (Table 1) of this HTC-AC sample, which shows a lower amount of fixed carbon (60.8 wt%) together with a higher amount of volatile carbon (33.5 wt%) respect to the other ACs. Once characterized from a physicochemical perspective, the synthesized ACs and the biochar HTC-PYRO were at the beginning electrochemically characterized by employing a three-electrode setup to evaluate their capacitive performances, using nickel foam as current collector. In Fig. 2, the corresponding CV curves of the ACs are reported. The

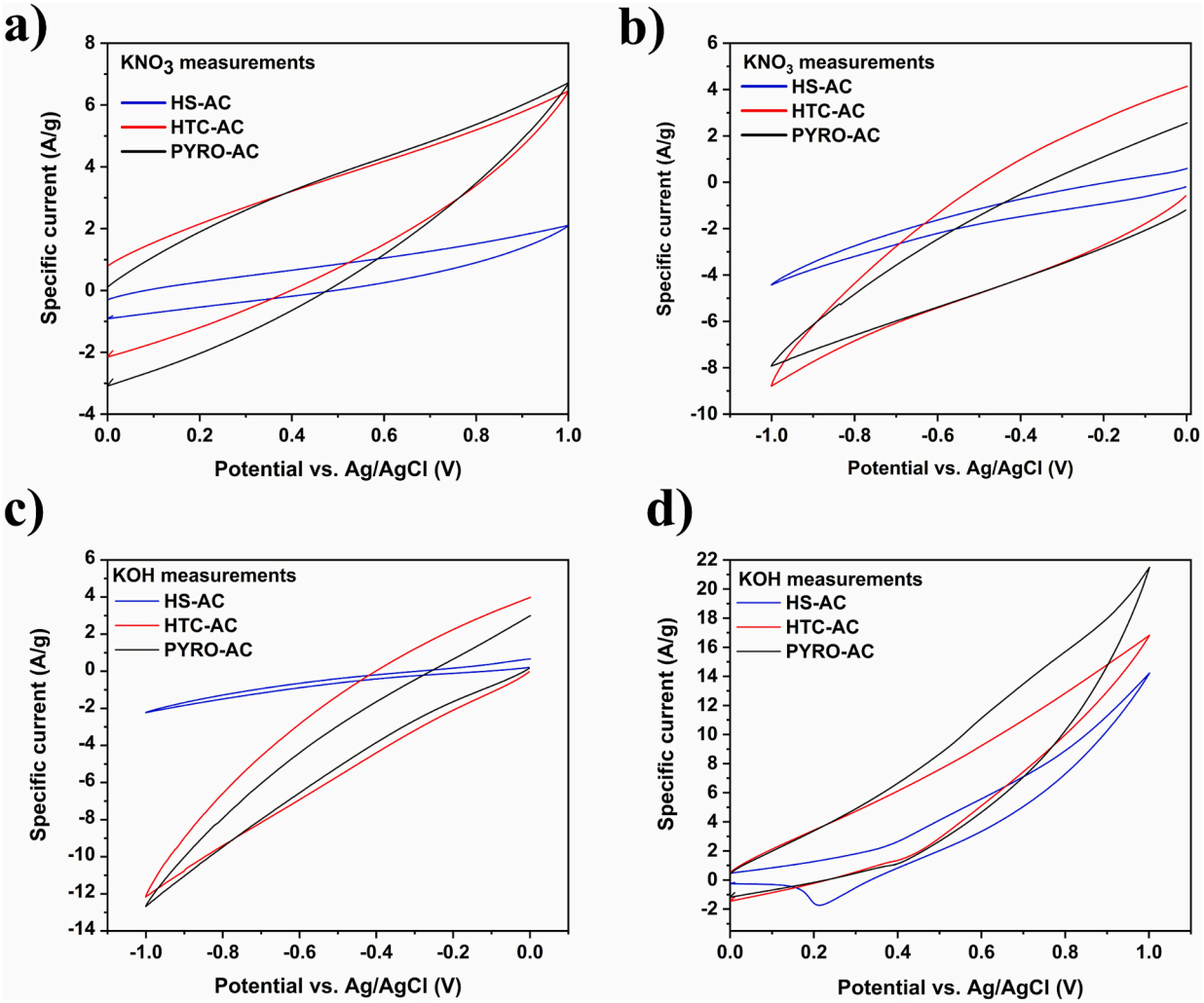

Fig. 2. CV curves of HS-AC, HTC-AC and PYRO-AC in a-b) KNO_3 and c-d) KOH (2.5 M) in the potential window between −1 to 0 V and 0 to 1 V at the scan rate of 0.1 V/s.

measurements were carried out working in KNO_3 (Fig. 2a and 2b) and KOH (Fig. 2c and 2d) as the electrolytes both chosen for their favorable balance of viscosity, ionic conductivity and stability (Mendhe and Panda, 2023; Chen et al., 2020; Nithya et al., 2013).

The CV scans were recorded within a potential window of −1 to 0 V and 0 to 1 V, using the scan rate of 0.1 V/s. The CV curves obtained for HTC-AC and PYRO-AC in both electrolytes displayed pseudo-rectangular shapes (Bograchev et al., 2023; Sharma and Chand, 2023). In particular, CV profiles for HTC-AC and PYRO-AC were more pronounced in KOH (Fig. 2c and 2d) than in KNO_3, reflecting the higher ionic conductivity of KOH (Mendhe and Panda, 2023). In the case of HS-AC, curves also show capacitive behavior in both cathodic and anodic zones, although in a minor magnitude compared with the other two ACs samples (HTC-AC and PYRO-AC). This can be attributed to the more developed porosity of the two samples resulting from the cascade thermal treatments. The correlation between tailored porosity and capacitive behavior is further confirmed by the unsatisfactory electrochemical performances ascertained for the pristine HTC-PYRO (Fig. S4), which is characterized by lower SSA (388 m^2/g) compared to the investigated ACs, highlighting the need to perform a chemical activation step to improve its performances (Lobato-Peralta et al., 2024; Licursi et al., 2023; Lee et al., 2021). On this basis, returning to ACs samples, the examination of the enlargement of the CV curves of HC-AS in KOH (Fig. S5) reveals that this sample exhibits minor Faradaic peaks, particularly in the anodic region, likely due to the redox activity of the nickel foam in alkaline media (Schrebler Guzmán et al., 1978). In fact, nickel foam may undergo oxidation from Ni^0 to Ni^{2+} and Ni^{3+} species, detected as two peaks of the $Ni(OH)_2$/NiO(OH) redox couple (Dojčinović et al., 2024). The corresponding C_s values are reported in Table S2 confirming the superior performance of HTC-AC and PYRO-AC, especially in KOH, where HTC-AC reached anodic C_s of 61 F/g and cathodic C_s of 35 F/g, while PYRO-AC achieved anodic C_s of 58 F/g and cathodic C_s of 37 F/g. On the other hand, lower C_s values were recorded in KNO_3, supporting the influence of its low electrolyte conductivity (Mendhe and Panda, 2023). In literature, it is possible to find a wide range of C_s values for ACs, generally in the range 30–400 F/g, in agreement with our data (Biesheuvel et al., 2018). Further insight was gained through GCD measurements performed in both electrolytes. The GCD curves for the AC samples (HS-AC, HTC-AC and PYRO-AC) are reported in Figs. S6, S7 and S8 where the deviation from an ideal triangular shape, especially in KOH, indicates the occurrence of faradaic processes. The GCD results recorded in KNO_3, presented in Fig. S9 as C_s versus the number of cycles, confirm the higher and more stable capacitance of HTC-AC and PYRO-AC compared to HS-AC. However, PYRO-AC showed slightly reduced cycling stability, potentially due to inconsistencies in current collector coverage. The corresponding C_s values (Table S3) are lower than those obtained from the CV curves (Table S2), confirming the presence of irreversible Faradaic processes, the contribution of which is considered in the calculation of C_s from CV curves, but not from charge and discharge cycles. Definitely, on the basis of the characterization and first electrochemical screening activity, HTC-AC and PYRO-AC samples result in the most promising ACs.

3.2. *Cu-doped ACs: physicochemical characterization and electrochemical behavior with aqueous electrolytes*

In order to improve the electrochemical performance, Cu-doping of the most interesting ACs, HTC-AC and PYRO-AC, was carried out, obtaining the corresponding Cu-HTC-AC and Cu-PYRO-AC with the aim of introducing copper oxides on the carbon surface with slight modifications to procedures reported in the literature (Saravanakumar et al., 2019; Zhan et al., 2021b). Initially, the Cu-doped samples were characterized by their morphological and physicochemical properties. SEM analysis was performed (Figs. S10 and S11) revealing for both samples the presence of carbon aggregates and the presence of copper oxides particles deposited on the AC surface. EDS analysis was carried out to confirm the presence of copper and the results are summarized in Table S4, resulting in line with what was expected. SSA measurements resulted to be 697 and 397 m^2/g for Cu-HTC-AC and Cu-PYRO-AC respectively (versus 1155 and 710 m^2/g of the corresponding precursors), attributable to the pore blockage of copper oxides. The Cu-HTC-AC isotherm, together with the corresponding cumulative pore volumes and the pore size distribution are reported in Fig. S12, where it can be observed that Cu-HTC-AC feature the same pore size distribution of its precursor (Fig. S2), but displaying different pores openings, as suggested to additional microporosity introduced by the copper oxide itself at 0.47 nm, and the absence of micropores at 1.43 nm (Fig. S12). Regarding the ultimate analysis data of the doped ACs, Cu-HTC-AC (C = 57.6 wt%, H = 2.4 wt%, N = 0.2 wt%, O = 22.5 wt%) and Cu-PYRO-AC (C = 70.0 wt%, H = 0.7 wt%, N = 0.6 wt%, O = 12.5 wt%), both samples show similar CHN contents respect to their undoped precursors (C = 60.0 wt%, H = 2.0 wt%, N = 0.1 wt% for HTC-AC and C = 74.3 wt%, H = 0.9 wt%, N = 0.7 wt% for PYRO-AC), whereas the O ones are lower (22.5 respect to 31.4 wt% for Cu-HTC-AC/HTC-AC and 12.5 respect to 18.0 wt% for Cu-PYRO-AC/PYRO-AC), due to the greater ash contribution which increases from 5.7 to 17.3 wt% for Cu-HTC-AC and from 6.1 to 16.2 wt% for Cu-PYRO-AC. In order to quantify the real amount in our Cu-doped ACs, ICP-OES analysis was carried out, finding Cu content of 5.6 and 5.8 wt% for Cu-HTC-AC and Cu-PYRO-AC, in agreement with the nominal values of 6.5 and 5.4 wt%, respectively. In addition, Raman and XRD analyses were performed to assess their structural properties. Raman spectrum of Cu-HTC-AC with normalized intensity with respect to the G peak (as a representative example of doped samples) together with the HTC-AC and PYRO-AC precursors, the correlation between peak positions and Full Width at Half Maximum (FWHM) and the deconvoluted spectra are all reported in Fig. 3.

From this first comparison, it is evident that the overall Id/Ig ratio is not sensibly varying among samples. The G peak, associated with the E2g vibrational mode, is positioned around 1580 cm^{-1}, while the D peak, corresponding to the A1g vibrational mode, appears around 1360 cm^{-1}. Furthermore, the Cu-HTC-AC samples a low intense peak at 215 cm^{-1} which seems to correspond to Cu_2O (Solache-Carranco et al., 2008). Deeper insight has revealed that the Raman feature of the carbon component of the investigated samples can be further deconvoluted into four modes named G1 and G2 under the G band, and D1 and D2 under the D one. These results are reported in Fig. 3c-d-e and peak data are summarized in Table S5. In this deconvolution, G1 and D1 are the ones closer to the typical Raman mode features of graphitic carbons: in fact, both G1 and D1 modes resulted in blue shifted with respect to the respective 1580 and 1350 cm^{-1} representative resonant modes, suggesting a compressive stress on the graphitic structure. According to the analysis reported in Fig. 3b, it is evident the stable position of both G1 and G2 peaks, around an average position of 1588.2 and 1564.5 cm^{-1}, respectively. Concerning the D1 and D2 peaks, D1 results closely dispersed around 1360.2 cm^{-1}, while D2 scatters around 1156.3 cm^{-1} with much pronounced dispersion also in terms of full width at half maximum (FWHM). According to Shimodaira *et al.*, G1 and D1 are due to the graphitic domains, while G2 and D2 are ascribed to amorphous carbons phases (Shimodaira and Masui, 2002). Due to the position of the D2 peak relatively far from the position of the expected D peak, it is reasonable to assume that such a vibrational mode can be attributed to something different with respect to the defective vibrational modes of amorphous-graphitic structures. According to Ferrari and Robertson, such a vibrational mode can be originated from the coexistence of sp^3 phase and conjugated non-aromatic polyenes, present as pending groups of graphitic platelets (Ferrari and Robertson, 2001). Henceforth, D2 does not account for evaluations. Nevertheless, its reduced intensity in the Cu-HTC-AC sample with respect to those in HTC-AC and PYRO-AC samples can be due to the presence of metal oxide surface functionalities. Following the interpretations of Shimodaira *et al.*, in Table S5 it is reported also the Ig2 to Ig1 ratio, whose values are in accordance with the authors concerning the graphitizable carbons activated with KOH,

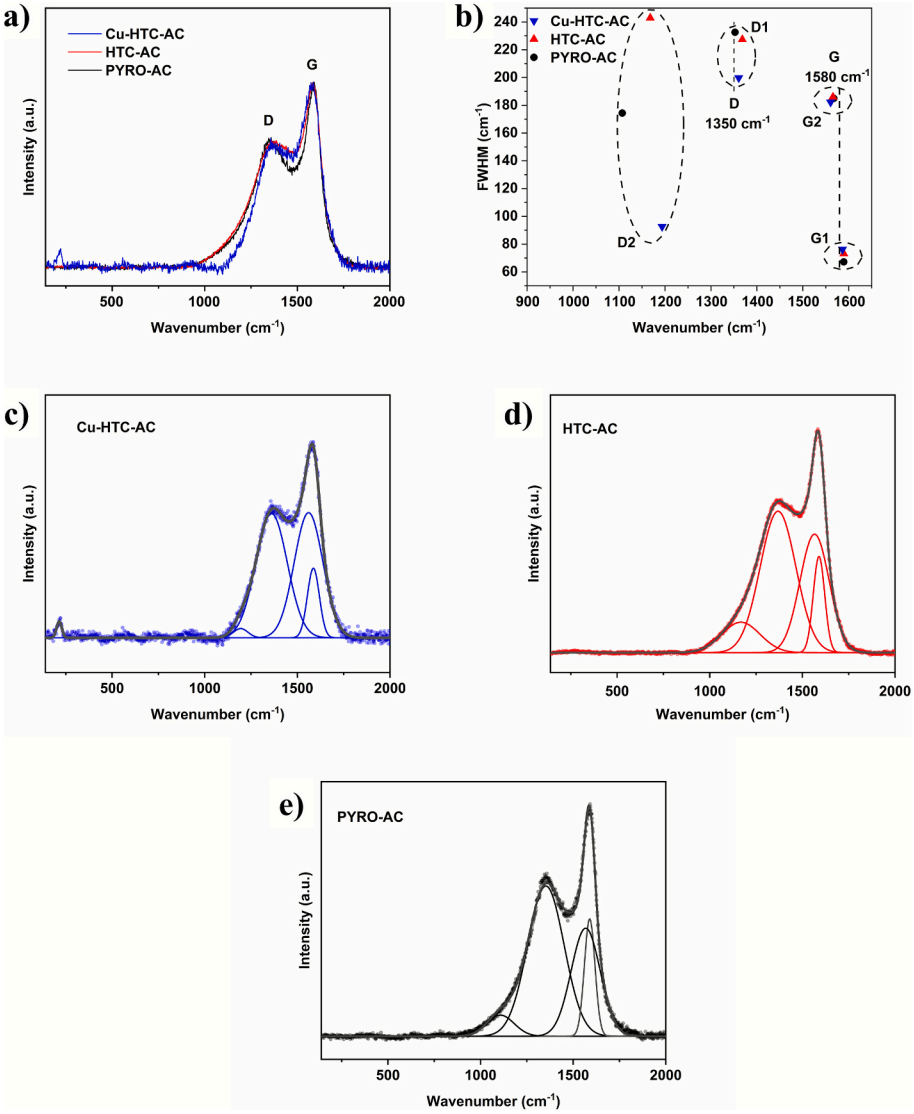

Fig. 3. Raman spectra of Cu-HTC-AC, HTC-AC and PYRO-AC. a) baseline corrected Raman spectra of the three different samples; b) correlation between peak positions and FWHM; c) Cu-HTC-AC, d) HTC-AC and e) PYRO-AC deconvoluted Raman spectra.

indicating that the presented results are characteristic of disordered carbons (Shimodaira and Masui, 2002). In this regard, in recent years, increasing attention has been devoted to the role of structural disorder in carbon materials, which has been shown to enhance energy storage performance in SCs. Unlike the conventional focus on pore size, recent studies demonstrate that disorder in nanoporous carbons can significantly improve ion storage efficiency and energy density (Liu et al., 2024; Zhang et al., 2024) and this correlation between carbon structure and electrochemical performance applies across different dimensionalities and morphologies (Xiao et al., 2021; Jiang et al., 2018).

To verify the crystalline phase of the copper oxides present, XRD analysis was performed on both Cu-doped samples obtaining the same results and on their corresponding precursors (Fig. S13). Fig. 4 illustrates the pattern ascertained for Cu-HTC-AC as representative example.

The pattern shows two large broad peaks in the range 2θ of 20-30°and 40-45°, which derive from the disordered carbons. Moreover, two crystallographic phases were detected: one with space group R-3c:H (167), that can be linked to the corundum phase of Al_2O_3 (as suggested by Table S4, where the EDS detected the presence of aluminum) and the second one, with larger crystalline domains, with a space group of Pn-3 m:1 (224) that, according to the chemistry of the sample, belongs to the cuprite phase of the copper (I) oxide Cu_2O. In this sample, the crystalline fraction of the corundum is of (32.512794 ± 1.7356137) % and that of the cuprite of (67.487206 ± 2.39865) %. According to the Rietveld refinement, the corundum crystallites are (758.8053 ± 90.78744) Å and those of the cuprite are (1694.7803 ± 75.72117) Å in size. Once characterized, Cu-doped samples, which resulted in terms of Cu_2O amount equal to 6.3 and 6.5 wt% for Cu-HTC-AC and Cu-PYRO-AC respectively, were electrochemically tested under the same conditions as in the previous experiments. In Fig. 5, the corresponding CV curves of the Cu-doped ACs are reported.

Focusing on the corresponding CV curves of the Cu-doped ACs, those acquired in KNO_3 (Fig. 5a and 5b) display a pseudo-rectangular shape with more pronounced sharp edges than their undoped precursors, indicating the presence of increased pseudocapacitive behavior of these materials, due to the presence of Cu_2O, thus confirming the improved electrical conductivity and charge storage capacity (Saravanakumar et al., 2019; Zhan et al., 2021b; Dabir et al., 2024). Between the two Cu-doped ACs, Cu-HTC-AC exhibits a wider curve than Cu-PYRO-AC, indicating better capacitive behavior. The same observations can be made for the curves acquired in KOH (Fig. 5c and 5d), where higher current density values were recorded compared to those in KNO_3, due to the superior ionic conductivity of KOH, as already evidenced for the undoped samples. The C_s values (Table S6), calculated from the CV,

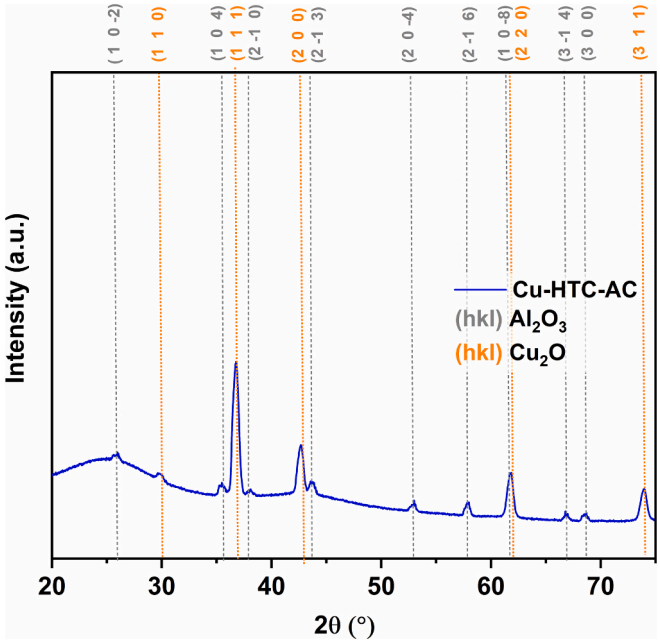

Fig. 4. XRD pattern of Cu-HTC-AC.

result higher for the sample Cu-HTC-AC with a notably high capacitance in the anodic region in KOH, highlighting its potential for further investigation of its electrochemical behavior. GCD measurements of the two Cu-doped ACs were performed under the same conditions previously employed and the GCD curves are reported in Figs. S14 and S15. Also in this case, the curve shape deviates from the ideal triangular form, as previously observed for the measurements of the undoped precursor. The GCD results recorded in KNO_3 are reported in Fig. S16 in terms of C_s values versus number of cycles. Cu-HTC-AC exhibits good C_s values and moderate stability during the cycles compared with Cu-PYRO-AC, indicating improved properties for SCs application. Again, GCD-derived C_s values (Table S7) were lower than those calculated from CV, consistent with trends already seen in the undoped samples. Altogether, on the basis of all results, it is possible to identify HTC-AC, PYRO-AC and Cu-HTC-AC as the most promising candidates for further electrochemical development and application in lithium-based storage and EDLC devices in organic electrolytes.

3.3. Applications of the most promising ACs (Cu-HTC-AC, HTC-AC and PYRO-AC) for Li-storage and EDLC devices in organic electrolytes

To further investigate the electrochemical properties of the most promising ACs, they were also tested with organic electrolytes and in this regard nickel foam was replaced with other current collectors, in particular copper and aluminum foils, due to issues encountered during

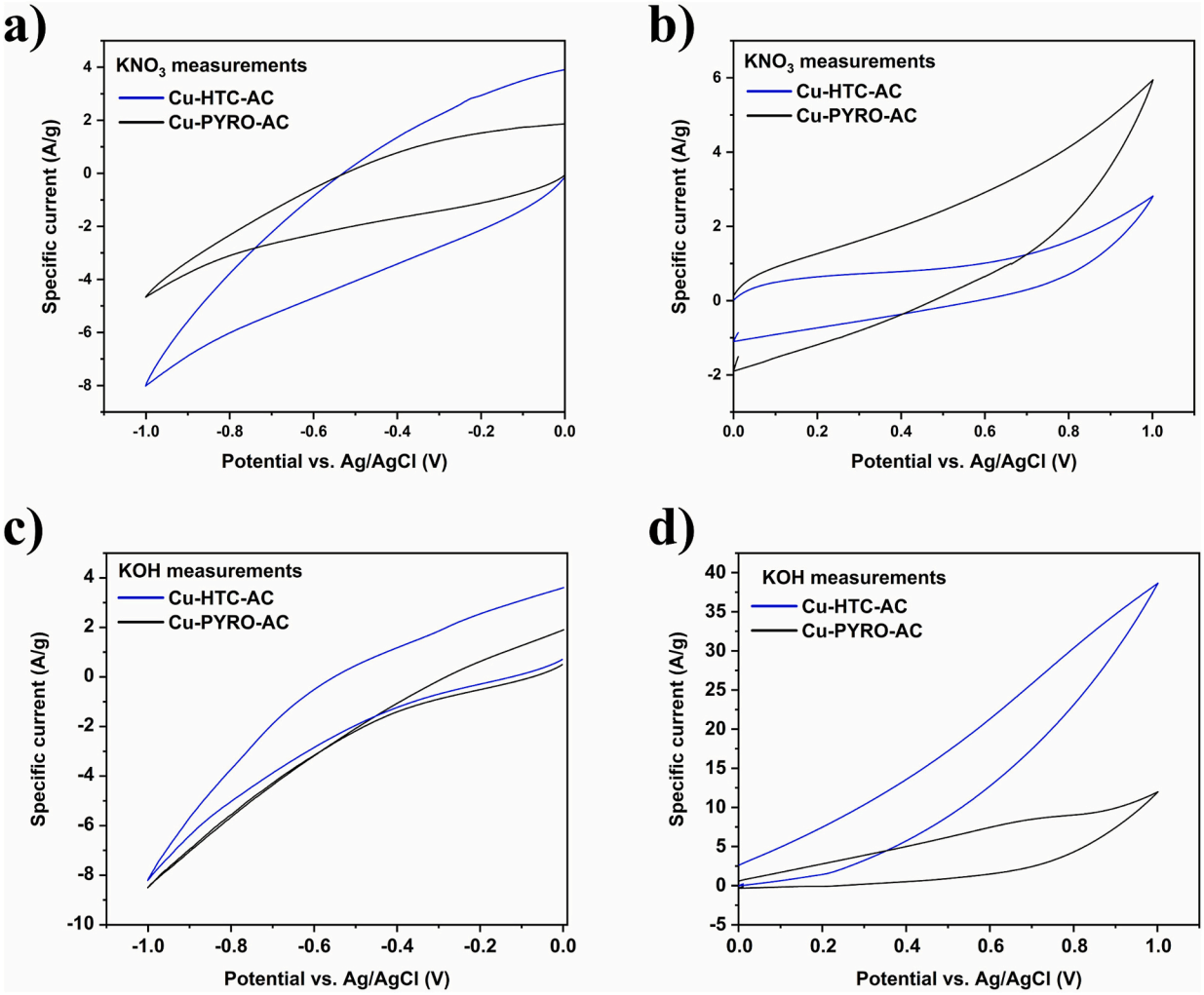

Fig. 5. CV curves of Cu-HTC-AC and Cu-PYRO-AC in a-b) KNO_3 and c-d) KOH (2.5 M) in the potential window between −1 to 0 V and 0 to 1 V at the scan rate of 0.1 V/s.

ink deposition and the occurrence of faradaic processes in aqueous electrolyte.

Considering the properties of our best samples, they were tested for lithium storage devices, evaluating their behavior as anode materials, suitable for use in lithium-ion batteries and/or lithium ion capacitors (Wang et al., 2021). For this reason, cathodic scan measurements were performed using a Swagelok cell and LP30 as electrolyte. All the ACs were deposited on copper current collectors providing manageable electrodes and the corresponding CV curves, recorded at the scan rate of 0.1 mV/s, together with the specific capacity evolution versus cycle number are reported in Fig. 6.

The results suggest that the sample Cu-HTC-AC features greater stability over cycling and this result is also found in literature where Cu_2O is exploited as passivating barrier for Li-ion graphite-based anodes (Fu et al., 2007), justifying its overall potential stability in these polarization conditions. According to the initial discharge specific capacity, the presence of Cu_2O appears to contribute to the capacity increase, as indicated by the overall higher specific capacity of Cu-HTC-AC compared to the undoped precursor. Conversely, the PYRO-AC sample exhibits a high initial specific capacity, with a progressive reduction during cycling. These experiments were run to probe eventual lithium storage properties and were not run in an optimized potential window. Based on the cathodic scan measurements performed, Cu-HTC-AC sample exhibits good stability over multiple cycles, on the basis of the literature assuming no significant changes to the copper phase (Bijani et al., 2007; Fu et al., 2007; Brisse et al., 2018), making it a promising candidate as anode materials for lithium storage devices.

Regarding the application in supercapacitor devices, despite the limited performance of PYRO-AC in previous tests, its powder was the only one suitable for fabricating a symmetric EDLC device in a two-electrode coin cell configuration with an aluminum current collector, whereas the other two samples could not be used due to coating adhesion difficulty on the selected collector. In details, the electrochemical performance in anodic polarization of Cu-HTC-AC samples was not addressed due to the known instability of copper oxides in anodic polarizations (Wu et al., 2010). The electrochemical results for PYRO-AC are reported in Fig. 7, including CV (Fig. 7a), coulombic efficiency and capacity retention from cyclic voltammetry (Fig. 7b), electrochemical impedance spectroscopy (Fig. 7c) and galvanostatic charge–discharge measurements, which evaluate the EDLC performance at different specific currents and at a single specific current for long-term cycling (Fig. 7d, 7e and 7f). On the basis of the achieved results a Ragone plot was derived to assess the sample's ability to deliver specific energy and specific power (Fig. 7g).

Fig. 7a shows the results of applying increasing scan rates on PYRO-AC with the potential window from 0 to 2.5 V. The upper voltage applied is lower if compared to that used in the work of Le Fevre *et al.*, who employed the same electrolyte and cycled their cell up to 2.7 V (Le Fevre et al., 2019). In our case, a low voltage was applied to prevent material degradation, given the low coulombic efficiency observed in the CV and GCD tests (Fig. 7b). The CV curve at 5 mV/s exhibits a quasi-rectangular shape (Fig. 7a), indicating that, although it is not an ideal EDLC (box-shaped CV), the material demonstrates capacitive behavior with C_s value of 55 F/g. This value is relatively high compared to the commercial YP80F, which gave 28 F/g at the same scan rate and electrolyte, but in a lower potential window of 0.1–2.3 V (Farm, 2020; Egun, et al., 2024). Another commercial product, the YP50F sample, exhibited C_s of 143 F/g at 10 mV/s, in half cell configuration (about. 35.7 F/g device) but, in that case, the test was carried out within 0–2 V voltage window employing acetonitrile as the electrolyte solvent, which is known to have higher conductivity at room temperature. As the scan rate increased, the CV curve of Fig. 7a changed, becoming more diagonal and oval-shaped, with sharper ends, characteristics of a resistive CV shape. This highlights that it is more difficult for the material to support high rates, hence the reduced area inside the curve. EIS was performed to identify the underlying reason for such behavior and the result is shown in Fig. 7c. A study by Kost *et al.* on carbon materials tested with different electrolyte combinations at varying temperatures showed that the Warburg line became more vertical as the temperature increased, as the influence of electrolyte conductivity became more significant (Kost, et al., 2024). In other studies that tested polymer electrolyte, which have poor conductivity at room temperature, by increasing the electrode conductivity, the Warburg line also became more vertical (Kiseleva, et al., 2024; Aziz, et al., 2019). Based on this, it can be concluded that, since in our experiment a reasonably conductive $TEABF_4$ 1 M in PC electrolyte was used, it can be said that the formation of the diffusive branch line suggest that the ions permeates with difficulty due to the electrode material itself (Dsoke, et al., 2013), also in accordance with the De Levie model of porous carbons where a distributed resistance may also appear in the solid electrode phase (de Levie, 1967). This causes overall resistive behavior. Moreover, the presence of a semi-circle suggests that the overall coated electrode material suffers from parasitic resistance due to the dried electrode non-uniformity.

From the above discussion, the parasitic resistance may be attributed to the heterogeneity of the PYRO-AC material. This results in a less than optimum charge percolation process on the material's surface, resulting in the cathode material itself being the source of resistance (Dsoke et al., 2013; Sun et al., 2014). These assumptions are further confirmed by the apparent non-hierarchical structure of the materials porosities. Indeed, given the presence of large and potentially resistive particles as well as

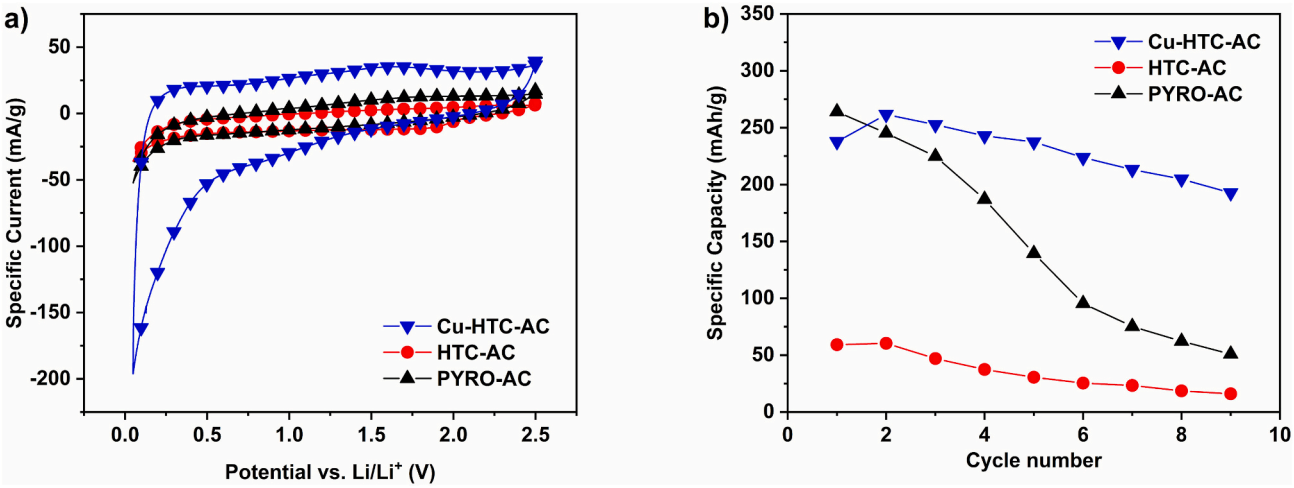

Fig. 6. CV curves (a) and specific capacity evolution versus cycle number (b) recorded at 0.1 mV/s in $LiPF_6$ 1 M in 1:1 (v:v) EC:DMC + 2 wt% VC.

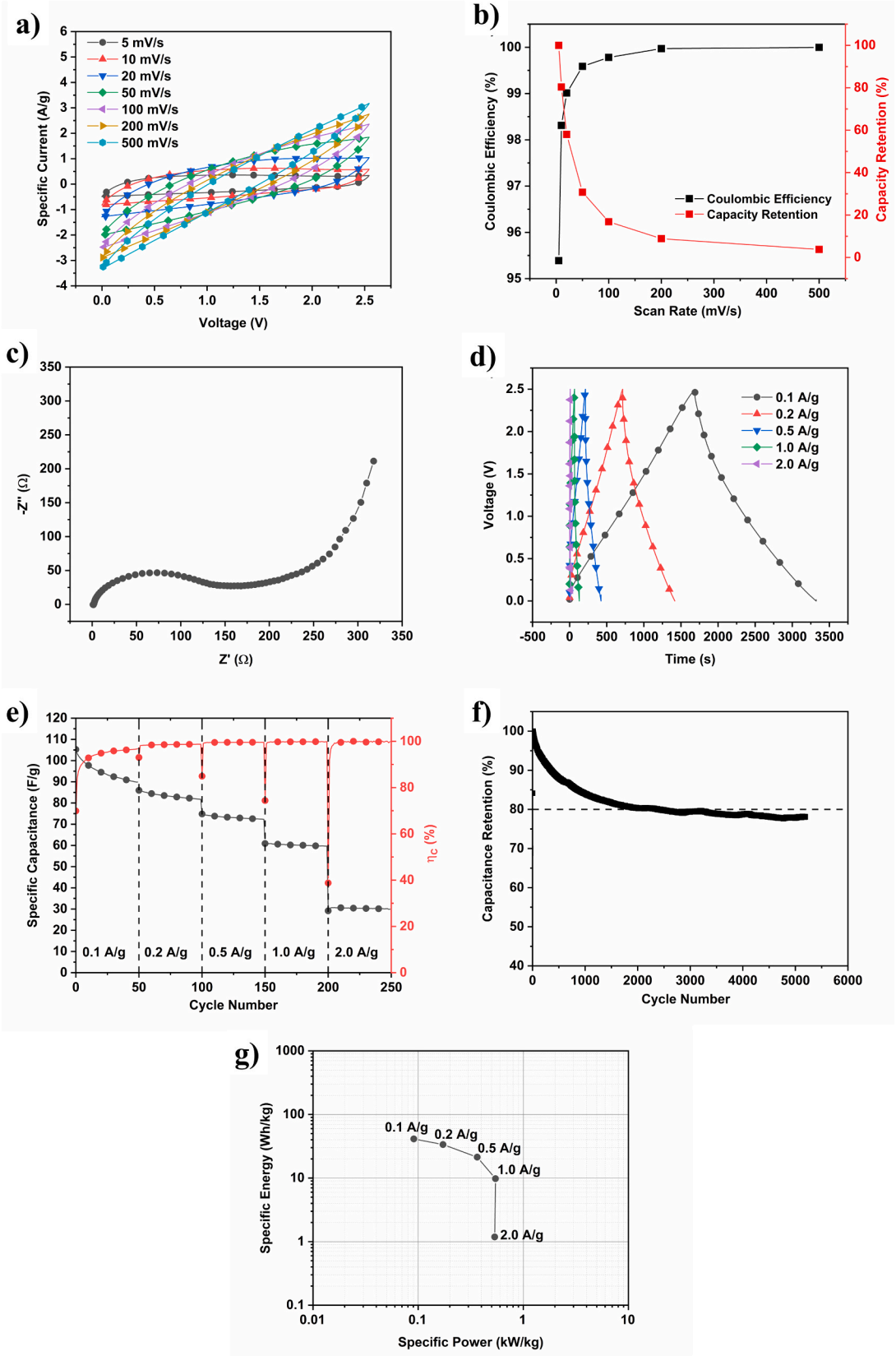

Fig. 7. Electrochemical results for PYRO-AC sample in the two-electrode coin cell system. a) CV curves; b) Coulombic efficiency and the capacity retention of CV tests; c) EIS of the EDLC device recorded at OCV; d) GCD profiles recorded at different current rates; e) Capacitance retention profile and coulombic efficiency variation; f) Results of the galvanostatic cyclability test performed at 1.0 A/g; g) Ragone plot derived from the GCD measurements.

the absence of mesopores suggested by the pore size distribution analyses (Fig. S3), it is reasonable to assume that ions are subject to tortuous paths within micropores. Reducing the particle size of PYRO-AC may enhance size uniformity and reduce parasitic contributions.

However, by benchmarking this result with literature results (Liu et al., 2025) which used HTC and chemical activation (KOH) to synthesize glucose-derived AC-tested using 1 M $TEABF_4$ in acetonitrile (ACN) electrolyte, it was possible to note that neither the number of processing steps nor a higher SSA necessarily leads to better-performing ACs for energy storage applications, but only an optimized process control is essential when producing ACs, including those from the waste HS.

The rate capability test is presented in Fig. 7d. All GCD curves display a well-defined triangular shape, with the total charge–discharge time decreasing as the specific current increases. As shown in Fig. 7e, and consistent with the CV results, the GCD measurements indicate a gradual reduction in C_s as the current rate rises. This fading capacity is likely due to inhibited charge diffusion and ion permeation, as discussed previously. At higher current rates, the ability of charge carriers to respond diminishes due to increased material resistance, which limits full utilization of the active surface area. In other words, the electrochemical kinetics of double-layer formation are constrained by the resistive behavior of the electrode at higher current densities. These effects may have been further aggravated by potential pore collapse, resulting from the multiple thermal treatments applied to the PYRO-AC sample. In addition to the charge–discharge profiles, GCD testing was also used to assess the material's durability over prolonged cycling (Fig. 7f), specifically by analyzing the capacitance retention across GCD cycles. Retention was calculated by dividing the discharge value of the nth cycle by that of the first cycle. As shown in Fig. 7f, capacitance retention declined steadily over the first 1500 cycles before stabilizing around 80%. This behavior is notable, as it contrasts with the typical continuous decline seen in many other cases and may be attributed to the surface reactivity of the carbon materials used.

Despite the instabilities, the Ragone plot reported in Fig. 7g presents remarkable specific energy density (40 Wh/kg at 0.1 A/g) and good power capabilities (700 W/kg at 2.0 A/g). Although the PYRO-AC sample features an outstanding C_s (estimated 220 F/g per electrode) with respect to commercial carbon materials, its power capability remains limited. As mentioned before, this material exhibits parasitic resistive behavior evident from EIS which prevents it from operating effectively at higher power rates. This limitation in power capabilities can be explained by considering the maximum power formula for generators, $P = V^2/(4R)$, where the R resistance value in this formula is the one proper of the adapted load condition and V is the voltage. At the different characterization rates, this resistance is closer to the internal resistance of the device, which is on order of hundreds of ohms, as indicated in the EIS plot (Fig. 7c). Consequently, the material cannot sustain higher power rates compared to commercially available reference materials due to its resistive nature and as previously mentioned, the synthesis process requires further improvement to enhance the performance of this AC. However, despite the relatively low voltage window (2.5 V) and in its current state PYRO-AC already showed remarkable C_s (55 F/g) value and specific energy density (40 Wh/kg), demonstrating the clear potential of HS waste to be used as electrode in energy storage devices. To conclude, in our hypothesis the PYRO-AC sample features a remarkable energy storage performance controlled more by the disorder level (Fig. 3e) rather than the SSA and pore size distribution (Fig. S3) as proved also by Raman analyses. Moreover, the potentially oxygenated surface and stressed sp2 domains can contribute to local increase of the material C_s, consequently its energy density.

4. Conclusion

In this work, several activated carbons were synthesized, employing an energy-efficient process, by alkaline activation of the hazelnut shell waste biomass through a cascade approach of both thermal and chemical treatment processes. The influence of each process, namely hydrothermal carbonization, pyrolysis and activation pyrolysis, was carefully evaluated for their electrochemical performances. Preliminary electrochemical measurements, adopting nickel foam as the current collector, showed interesting results for the HTC-AC and PYRO-AC samples. Further improvement of electrochemical performances was achieved through copper (I) oxide doping of the most interesting ACs, achieving the best specific capacitance in the case of Cu-HTC-AC (123 F/g). Further electrochemical measurements were performed by changing current collectors and evaluating the most promising samples for lithium ion and EDLC storage capability. The Cu-HTC-AC sample exhibits great stability over multiple cycles in standard Li-ion electrolyte and high specific capacity value (250 mAh/g), making it a promising candidate as anode materials for lithium storage devices. The other promising sample PYRO-AC was tested in EDLC device, which surprisingly gave a specific capacitance value of 55 F/g in symmetrical cell configuration, value higher than those achieved for commercial activated carbons (up to 30 F/g). According to the performed characterization, the possible explanation for this remarkable performance of PYRO-AC leading to 40 Wh/kg in symmetrical device can be explained according to the current disorder theory. In conclusion, this work shows an effective and energy-efficient route for converting agricultural or industrial waste residues into functional carbonaceous materials with promising applications in the energy storage sector, promoting the re-use of waste resources in the circular economy perspective.

CRediT authorship contribution statement

Stefania Volante: Writing – original draft, Methodology, Investigation, Formal analysis, Data curation. **Rif Atussaufiyah:** Investigation, Data curation. **Federico Maria Vivaldi:** Writing – original draft, Methodology, Investigation, Data curation. **Pietro Zaccagnini:** Writing – original draft, Methodology, Investigation, Data curation. **Mara Serrapede:** Writing – review & editing, Investigation. **Andrea Lamberti:** Writing – review & editing, Resources. **Anna Maria Raspolli Galletti:** Writing – review & editing, Resources. **Federico Bella:** Writing – review & editing, Resources, Methodology, Data curation. **Fabio Di Francesco:** Writing – review & editing, Resources. **Domenico Licursi:** Writing – original draft, Supervision, Methodology, Investigation, Data curation. **Claudia Antonetti:** Writing – review & editing, Supervision, Resources, Methodology, Funding acquisition, Data curation, Conceptualization.

Declaration of competing interest

The authors declare that they have no known competing financial interests or personal relationships that could have appeared to influence the work reported in this paper.

Acknowledgements

This study was carried out within the MOST— Sustainable Mobility Center and received funding from the European Union Next-GenerationEU (PIANO NAZIONALE DI RIPRESA E RESILIENZA (PNRR)-MISSIONE 4, COMPONENTE 2, INVESTIMENTO 1.4-D.D.1033 17/06/2022, CN00000023). This manuscript reflects only the authors' views and opinions; neither the European Union nor the European Commission can be considered responsible for them. The University of Pisa is acknowledged for the support under the project "Microwave Assisted Approaches for Heritage Science, Environment, and Energy" (PRA_2022_58). The authors thank Marco Martinelli and David Michelotti for the technical support provided.

Appendix A. Supplementary data

Supplementary data to this article can be found online at https://doi.

org/10.1016/j.wasman.2026.115363.

Data availability

Data will be made available on request.

References

Ansari, M.Z., Hablb, F., Gupta, J., Alsubale, A.S., Barsoum, I., Alfantazl, A., Yatoo, M.A., Ahmad, Z., Hussaln, I., 2024. Frontiers in metal-organic frameworks: innovative nanomaterials for next-generation supercapacitors. Adv. Compos. Hybrid Mater. 7, 215. https://doi.org/10.1007/s42114-024-00996-2.

Aziz, M.A., Shah, S.S., 2023. Biomass-based supercapacitors: design, fabrication and sustainability. John Wiley & Sons Inc, pp. 329–346.

Aziz, S.B., Hamsan, M.H., Abdullah, R.M., Kadir, M.F.Z., 2019. A promising polymer blend electrolytes based on chitosan: methyl cellulose for EDLC application with high specific capacitance and energy density. Mol 24, 2503. https://doi.org/10.3390/molecules24132503.

Beknalkar, S.A., Teli, A.M., Harale, N.S., Patil, D.S., Pawar, S.A., Shin, J.C., Patil, P.S., 2021. Fabrication of high energy density supercapacitor device based on hollow iridium oxide nanofibers by single nozzle electrospinning. Appl. Surf. Sci. 546, 149102. https://doi.org/10.1016/j.apsusc.2021.149102.

Bhat, S.A., Kumar, V., Kumar, S., Yudhana, A., Atabani, A.E., Badruddin, I.A., Chae, K.J., 2023. Supercapacitors production from waste: a new window for sustainable energy and waste management. Fuel 337, 127125. https://doi.org/10.1016/j.fuel.2022.127125.

Bhojane, P., 2022. Recent advances and fundamentals of pseudocapacitors: materials, mechanism, and its understanding. J. Energy Storage. 45, 103654. https://doi.org/10.1016/j.est.2021.103654.

Biesheuvel, P.M., Porada, S., Dykstra, J.E., 2018. [Online]. Available: http://arxiv.org/abs/1809.02930.

Bijani, S., Gabás, M., Martínez, L., Ramos-Barrado, J.R., Morales, J., Sánchez, L., 2007. Nanostructured Cu_2O thin film electrodes prepared by electrodeposition for rechargeable lithium batteries. Thin Solid Films 515, 5505–5511. https://doi.org/10.1016/j.tsf.2007.01.016.

Bograchev, D.A., Volfkovich, Y.M., Martemianov, S., 2023. Diagnostics of supercapacitors using cyclic voltammetry: modeling and experimental applications. JEAC 935, 117322. https://doi.org/10.1016/j.jelechem.2023.117322.

Borchardt, L., Oschatz, M., Kaskel, S., 2014. Tailoring porosity in carbon materials for supercapacitor applications. Mater. Horiz. 1, 157–168. https://doi.org/10.1039/C3MH00112A.

Brisse, A.L., Stevens, P., Toussaint, G., Crosnier, O., Brousse, T., 2018. Performance and limitations of Cu_2O:graphene composite electrode materials for aqueous hybrid electrochemical capacitors. Electrochim. Acta 279, 161–167. https://doi.org/10.1016/j.electacta.2018.04.202.

Chen, K., Xue, D., 2013. Room-temperature chemical transformation route to CuO nanowires toward high-performance electrode materials. J. Phys. Chem. C 117, 22576–22583. https://doi.org/10.1021/jp4081756.

Chen, D., Li, Z., Jiang, J., Wu, J., Shu, N., Zhang, X., 2020. Influence of electrolyte ions on rechargeable supercapacitor for high value-added conversion of low-grade waste heat. J. Power Sources 465, 228263. https://doi.org/10.1016/j.jpowsour.2020.228263.

Dabir, M.P., Masoudpanah, S.M., Bafghi, M.S., Mamizadeh, M., 2024. Tuning the composition of CuO/Cu_2O composite powders via solution combustion method for supercapacitor application. MSE b. 306, 117479. https://doi.org/10.1016/j.mseb.2024.117479.

Dallaev, R., 2025. Conductive polymer thin films for energy storage and conversion: supercapacitors, batteries, and solar cells. Polymers 17, 2346. https://doi.org/10.3390/polym17172346.

Dangbegnon, J., Garino, N., Angelozzi, M., Laurenti, M., Seller, F., Serrapede, M., Zaccagnini, P., Moras, P., Cocuzza, M., Ouisse, T., Pazniak, H., Gonzalez-Julian, J., Sheverdyaeva, P., Polina, M., Di Vito, A., Pedico, A., Pirri, C.F., Lamberti, A., 2023. High-performance novel asymmetric MXene@CNT//N-doped CNT flexible hybrid device with large working voltage for energy storage. J. Energy Storage. 63, 106975. https://doi.org/10.1016/j.est.2023.106975.

De Levie, R., 1967. Advances in electrochemistry and electrochemical engineering. Wiley-Interscience, New York 6, 329.

Dojčinović, M.P., Stojković Simatović, I., Nikolić, M.V., 2024. Supercapacitor Electrodes: Is Nickel Foam the Right Substrate for Active Materials? Materials 17, 1292. https://doi.org/10.3390/ma17061292.

Dsoke, S., Tian, X., Täubert, C., Schlüter, S., Wohlfahrt-Mehrens, M., 2013. Strategies to reduce the resistance sources on electrochemical double layer capacitor electrodes. J. Power Sources 238, 422–429. https://doi.org/10.1016/j.jpowsour.2013.04.031.

Egun, I.L., Hu, D., He, H., Chen, G.Z., 2024. Molten base carbonisation and activation of bamboo shoots to generate capacitive carbon. Proceedings 105, 37. https://doi.org/10.3390/proceedings2024105037.

Elmouwahidi, A., Bailón-García, E., Pérez-Cadenas, A.F., Maldonado-Hódar, F.J., Carrasco-Marín, F., 2017. Activated carbons from KOH and H3PO4-activation of olive residues and its application as supercapacitor electrodes. Electrochim. Acta 229, 219–228. https://doi.org/10.1016/j.electacta.2017.01.152.

Farm, Y., PhD thesis, University of Sheffield (UK), 2020.

Ferrari, A.C., Robertson, J., 2001. Origin of the 1150 cm^{-1} Raman mode in nanocrystalline diamond. Phys. Rev. B 63, 121405.

Fu, L.J., Gao, G., Zhang, T., Cao, Q., Yang, L.C., Wu, Y.P., Holze, R., 2007. Effect of Cu_2O on graphite as anode material of lithium ion battery in PC-based electrolyte. J. Power Sources 171, 904–907. https://doi.org/10.1016/j.jpowsour.2007.05.099.

Gao, Y., Yue, Q., Gao, B., Li, A., 2020. Insight into activated carbon from different kinds of chemical activating agents: a review. Sci. Total Environ. 746, 141094. https://doi.org/10.1016/j.scitotenv.2020.141094.

https://hazelnuthub.com/2024-top-5-hazelnut-producing-countries/ (accessed 20-06-25).

Hegde, S.S., Bhat, B.R., 2023. Solid waste-derived carbon materials for electrochemical capacitors. In: Inamuddin, A.T., Adnan, S.M. (Eds.), Sustainable Materials for Electrochemical Capacitors. Wiley, Hoboken (USA), pp. 19–31. https://doi.org/10.1002/9781394167104.ch2.

Hegde, S.S., Shivakumar, B.R., Mishra, P., Dalimba, U., Ahmed, M.U., Santos, G.N., 2024. A novel and ultrasensitive high-surface porous carbon-based electrochemical biosensor for early detection of dengue virus. Biosens. Bioelectron.: X 20, 100525. https://doi.org/10.1016/j.biosx.2024.100525.

Inagaki, M., Konno, H., Tanaike, O., 2010. Carbon materials for electrochemical capacitors. J. Power Sources 195, 7880–7903. https://doi.org/10.1016/j.jpowsour.2010.06.036.

Jiang, L., Sheng, L., Fan, Z., 2018. Biomass-derived carbon materials with structural diversities and their applications in energy storage. Sci. China Mater. 61, 133–158. https://doi.org/10.1007/s40843-017-9169-4.

Kiseleva, E.A., Zhurilova, M.A., Kochanova, S.A., Shkolnikov, E.J., Tarasenko, A.B., Zaitseva, O.V., Uryupina, O.V., Valyano, G.V., 2024. Influence of carbon conductive additives on electrochemical double-layer supercapacitor parameters. J. Phys. Conf. Ser. 946, 012030. https://doi.org/10.1088/1742-6596/946/1/012030.

Kost, D.R., Kreth, F.A., Balducci, A., 2024. Post-mortem gas chromatography-mass spectrometry analysis of aging processes in acetonitrile-based supercapacitors. ChemElectroChem 11, e202300823. https://doi.org/10.1002/celc.202300823.

Lan, D., Chen, M., Liu, Y., Liang, Q., Tu, W., Chen, Y., Liang, J., Qiu, F., 2020. Preparation and characterization of high value-added activated carbon derived from biowaste walnut shell by KOH activation for supercapacitor electrode. J. Mater. Sci.: Mater Electron 31, 18541–18553. https://doi.org/10.1007/s10854-020-04398-0.

Lee, K.S., Seo, Y.J., Jeong, H.T., 2021. Capacitive behavior of functionalized activated carbon-based all-solid-state supercapacitor. Carbon Lett. 31, 1041–1049. https://doi.org/10.1007/s42823-020-00219-w.

Le Fevre, L.W., Fields, R., Redondo, E., Todd, R., Forsyth, A.J., Dryfe, R.A.W., 2019. Determining realistic electrochemical stability windows of electrolytes for electrical double-layer capacitors. J. Power Sources 424, 52–60. https://doi.org/10.1002/batt.202000009.

Licursi, D., Antonetti, C., Fulignati, S., Vitolo, S., Puccini, M., Ribechini, E., Bernazzani, L., Raspolli Galletti, A.M., 2017. In-depth characterization of valuable char obtained from hydrothermal conversion of hazelnut shells to levulinic acid. Biores. Technol. 244, 880–888. https://doi.org/10.1016/j.biortech.2017.08.012.

Licursi, D., Antonetti, C., Di Fidio, N., Fulignati, S., Benito, P., Puccini, M., Vitolo, S., Raspolli Galletti, A.M., 2023. Waste Manag. 168, 235–245. https://doi.org/10.1016/j.wasman.2023.06.012.

Liu, X., Lyu, D., Merlet, C., Leesmith, M.J.A., Hua, X., Xu, Z., Grey, C.P., Forse, A.C., 2024. Structural disorder determines capacitance in nanoporous carbons. Science 384, 321–325. https://doi.org/10.1126/science.adn624.

Liu, X., Hunter, R., Xu, Z., Lahrar, E.H., Merlet, C., Grey, C., Titirici, M.M., Forse, A., 2025. Highly disordered nanoporous carbons for enhanced energy storage in supercapacitors. ChemRxiv. https://doi.org/10.26434/chemrxiv-2025-4wvlj.

Lobato-Peralta, D.R., Okoye, P.U., Alegre, C., 2024. A review on carbon materials for electrochemical energy storage applications: state of the art, implementation, and synergy with metallic compounds for supercapacitor and battery electrodes. J. Power Source. 617, 235140. https://doi.org/10.1016/j.jpowsour.2024.235140.

Mascarenhas, F.J., Hegde, S.S., Bhat, B.R., 2023. Supercapattery: an electrochemical storage device. In: Inamuddin, A.T., Adnan, S.M. (Eds.), Sustainable Materials for Electrochemical Capacitors. Wiley, Hoboken (USA), pp. 279–290. https://doi.org/10.1002/9781394167104.ch11.

Mendhe, A., Panda, H.S., 2023. A review on electrolytes for supercapacitor device. Discov. Mater. 3, 29. https://doi.org/10.1007/s43939-023-00065-3.

Moosavifard, S.E., El-Kady, M.F., Rahmanifar, M.S., Kaner, R.B., Mousavi, M.F., 2015. Designing 3D highly ordered nanoporous CuO electrodes for high-performance asymmetric supercapacitors. ACS Appl. Mater. Interfaces 7, 4851–4860. https://doi.org/10.1021/am508816t.

Nithya, V.D., Selvan, R.K., Kalpan, D., Vasylechko, L., Sanjeeviraj, C., 2013. Synthesis of Bi_2WO_6 nanoparticles and its electrochemical properties in different electrolytes for pseudocapacitor electrodes. Electrochim. Acta 109, 720–731. https://doi.org/10.1016/j.electacta.2013.07.138.

Olabi, A.G., Abbas, Q., Abdelkareem, M.A., Alami, A.H., Mirzaeian, M., Sayed, E.T., 2023. Carbon-based materials for supercapacitors: recent progress, challenges and barriers. Batteries. 9, 19. https://doi.org/10.3390/batteries9010019.

Pathak, M., Cygan, P.J., Bhatt, R.C., Tatrari, G., Rana, S., Arya, M.C., Sahoo, N.G., 2024. High energy density supercapacitors: an overview of efficient electrode materials, electrolytes, design, and fabrication. Chem. Rec. 24, e202300236. https://doi.org/10.1002/tcr.202300236.

Pedico, A., Lamberti, A., Gigot, A., Fontana, M., Bella, F., Rivolo, P., Cocuzza, M., Pirri, C. F., 2018. High-performing and stable wearable supercapacitor exploiting rGO aerogel decorated with copper and molybdenum sulfides on carbon fibers. ACS Appl. Energy Mater. 1, 4440–4447. https://doi.org/10.1021/acsaem.8b00904.

Pérez-Armada, L., Rivas, S., González, B., Moure, A., 2019. Extraction of phenolic compounds from hazelnut shells by green processes. J. Food Eng. 255, 1–8. https://doi.org/10.1016/j.jfoodeng.2019.03.008.

Poonam, S.K., Arora, A., Tripathi, S.K., 2019. Review of supercapacitors: materials and devices. J. Energy Storage. 21, 801–825. https://doi.org/10.1016/j.est.2019.01.010.
Reina, M., Serrapede, M., Zaccagnini, P., Pedico, A., Castellino, M., Bianco, S., Ouisse, T., Pazniak, H., Gonzalez-Julian, J., Lamberti, A., 2023. Decoration of laser induced graphene with MXene and manganese oxide for fabrication of a hybrid supercapacitor. Electrochim. Acta 468, 143163. https://doi.org/10.1016/j.electacta.2023.143163.
Sajjad, M., Lu, W., 2021. Covalent organic frameworks based nanomaterials: design. synthesis, and current status for supercapacitor applications: a review. J. Energy Storage 39, 102618. https://doi.org/10.1016/j.est.2021.102618.
Saravanakumar, B., Radhakrishnan, C., Ramasamy, M., Kaliaperumal, R., Britten, A.J., Mkandawire, M., 2019. Copper oxide/mesoporous carbon nanocomposite synthesis, morphology and electrochemical properties for gel polymer-based asymmetric supercapacitors. JEAC 852, 11350. https://doi.org/10.1016/j.jelechem.2019.113504.
Schrebler Guzmán, R.S., Vilche, J.R., Arvía, A.J., 1978. Rate processes related to the hydrated nickel hydroxide electrode in alkaline solutions. J. Electrochem. Soc. 125, 1578. https://doi.org/10.1149/1.2131247.
Sharma, S., Chand, P., 2023. Supercapacitor and electrochemical techniques: a brief review. Results Chem. 5, 100885. https://doi.org/10.1016/j.rechem.2023.100885.
Shimodaira, N., Masui, A., 2002. Raman spectroscopic investigations of activated carbon materials. J. Appl. Phys. 92, 902–909. https://doi.org/10.1063/1.1487434.
Solache-Carranco, H., Juárez-Díaz, G., Galván-Arellano, M., Martínez-Juárez, J., Romero-Paredes, G., Peña-Sierra, R., 2008. Raman Scattering and Photoluminescence Studies on Cu_2O. In: 5th International Conference on Electrical Engineering, Computing Science and Automatic Control, pp. 421–424.
https://www.statista.com/statistics/1030790/tree-nut-global-production-by-type/ (accessed 20-06-2025).
Subramani, K., Sudhan, N., Karnan, M., Sathish, M., 2017. Orange peel derived activated carbon for fabrication of high-energy and high-rate supercapacitors. ChemistrySelect 2, 11384–11392. https://doi.org/10.1002/slct.201701857.
Sun, X.Z., Huang, B., Zhang, X., Zhang, D.C., Zhang, H.T., Ma, Y.W., 2014. Experimental investigation of electrochemical impedance spectroscopy of electrical double layer capacitor. Acta Phys. Chim. Sin. 30, 2071–2076. https://doi.org/10.3866/PKU.WHXB201408292.
Wang, Y., Zhang, L., Hou, H., Xu, W., Duan, G., He, S., Liu, K., Jiang, S., 2021. Recent progress in carbon-based materials for supercapacitor electrodes: a review. J. Mater. Sci. 56, 173–200. https://doi.org/10.1007/s10853-020-05157-6.
Wojdyr, M., 2010. Fityk: a general-purpose peak fitting program. J. Appl. Cryst. 43, 1126–1128 [reprint].
Wu, L., Tsui, L.K., Swami, N., Zangari, G., 2010. Photoelectrochemical stability of electrodeposited Cu_2O films. J. Phys. Chem. C 114, 11551–11556. https://doi.org/10.1021/jp103437y.
Xiao, J., Han, J., Zhang, C., Ling, G., Kang, F., Yang, Q.H., 2021. Dimensionality, function and performance of carbon materials in energy storage devices. Adv. Energy Mater. 12 (4), 2100775. https://doi.org/10.1002/aenm.202100775.
Xie, Y., Zhang, D., Jati, G.N.P., Yang, R., Zhu, W., Li, W., Marin, E., Pezzotti, G., 2021. Effect of structural and compositional alterations on the specific capacitance of hazelnut shell activated carbon. Colloids Surf A Physicochem Eng Asp 625, 126951. https://doi.org/10.1016/j.colsurfa.2021.126951.
Yang, L., Feng, Y., Cao, M., Yao, J., 2019. Two-step preparation of hierarchical porous carbon from KOH-activated wood sawdust for supercapacitor. Mater. Chem. Phys. 238, 121956. https://doi.org/10.1016/j.matchemphys.2019.121956.
Yuan, C., Xu, H., El-kodhary, S.A., Ni, G., Esakkimuthu, S., Zhong, S., Wang, S., 2024. Recent advances and challenges in biomass-derived carbon materials for supercapacitors: a review. Fuel 362, 130795. https://doi.org/10.1016/j.fuel.2023.130795.
Zhan, Y., Zhou, H., Guo, F., Tian, B., Du, S., Dong, Y., Qian, L., 2021a. Preparation of highly porous activated carbons from peanut shells as low-cost electrode materials for supercapacitors. J. Energy Storage. 34, 102180. https://doi.org/10.1016/j.est.2020.102180.
Zhan, Y., Bai, J., Guo, F., Zhou, H., Shu, R., Yu, Y., Qian, L., 2021b. Facile synthesis of biomass-derived porous carbons incorporated with CuO nanoparticles as promising electrode materials for high-performance supercapacitor applications. J. Alloy. Compd. 885, 161014. https://doi.org/10.1016/j.jallcom.2021.161014.
Zhang, H., Zhang, Y., Wen, Z., 2024. Disorder over pore size: boosting supercapacitor efficiency. Angew. Chem. Int. Ed. 63 (49), e202411039. https://doi.org/10.1002/anie.202411039.
Zheng, J.P., Cygan, P.J., Jow, T.R., 1995. Hydrous ruthenium oxide as an electrode material for electrochemical capacitors. J. Electrochem. Soc. 142, 2699. https://doi.org/10.1149/1.2050077.